Computational Materials Science 273 (2026) 114909

Contents lists available at ScienceDirect

Computational Materials Science

journal homepage: www.elsevier.com/locate/commatsci

Full length article

Molecular insights into inelasticity and fracture mechanics of nanostructured porous carbon

Hemangi Patel [a,b], Barbara Milow [a,b], Ameya Rege [a,c,*]

[a] Institute of Frontier Materials on Earth and in Space, German Aerospace Center (DLR), Linder Höhe, 51147, Cologne, Germany
[b] Department of Inorganic and Materials Chemistry, University of Cologne, Greinstr. 4-6, 50939, Cologne, Germany
[c] Department of Mechanics of Solids, Surfaces & Systems, University of Twente, PO Box 217, Enschede, 7500 AE, The Netherlands

ARTICLE INFO

Keywords:
Molecular dynamics
Mechanical properties
Fracture properties
Nanostructured porous carbon

ABSTRACT

Nanostructured porous carbon materials are gaining significant interest for a wide range of applications, particularly as electrode materials for electrochemical storage. In this work, the mechanical and fracture properties of nanostructured porous carbon are investigated using all atom molecular dynamics simulations. The models are generated using the methodology developed in our previous study (Patel et al., 2024). First, the effect of density on tensile deformation up to fracture is investigated. To further study the fracture behaviour, tensile deformation on notched systems was simulated and quantified by calculating the fracture toughness, K_{IC} and the critical energy release rate, G_C. As the crack length to height ratio, a/h increases, the fracture strength, σ_f decreases. The K_{IC} and G_C increases with a/h. To analyse the structural response to compaction, the inelastic behaviour was investigated by conducting uniaxial compression tests, particularly those under cyclic loading with increments in maximal applied strain per cycle. The increase in dissipated energy along with increasing residual deformation suggest very large plastic-like deformation. Pronounced tension–compression asymmetry is reported. The present investigations offer an initial yet comprehensive molecular-level understanding of the mechanical response of nanostructured porous carbon.

1. Introduction

Nanostructured porous carbon materials are gaining increasing attention owing to their unique physical properties like high specific surface area, low density and high electrical conductivity. These make them attractive for a wide range of applications such as batteries, fuel cells, supercapacitors, and gas storage [1–5]. Carbon aerogels belong to this class of materials and are synthesised by carbonisation of organic aerogels under inert gas conditions [6]. Several studies on the development of carbon aerogels with varying mechanical and structural properties have been reported [7–10]. Owing to their pore structure, with pore sizes smaller than 5 nm, they are excellent potential candidates as electrode material for metal-sulphur batteries [2]. However, for such applications, it is essential for the microstructure of the aerogels, at a nanometer scale, to remain flexible. Charging–discharging cycles lead to volumetric expansion–contraction of the sulphur which generates significant stresses in the carbon backbone. Several efforts have been ongoing to tailor the nanostructure of carbon aerogels such that it remains mechanically flexible under cyclic deformation for the intended electrode application [2,11]. The nanoscale mechanics of such materials remains poorly understood making optimisation for the mechanical properties a challenging task. At pore sizes below 1 nm, molecular mechanics plays an important role, and molecular simulations show promising potential.

After the first few studies on studying crack propagation using molecular dynamics (MD) [12], and following the advent of massively parallel computers, extensive research has been conducted to study the fracture mechanics of materials at the molecular level [13–17]. Mylvaganam and Yang [18] studied the tensile properties of carbon nanotubes using the Tersoff–Brenner potential. They further explored the propagation of necking along the tube and one-atom-chain formation for both armchair and zigzag nanotubes. Yang et al. [19] studied the mechanical and fracture properties of activated carbon. They showed that for the case of activated carbon, the fracture appears adjacent to the non-hexagonal ring defects and at the edge of the carbon wall frame grows vertically along the tensile axis. The effect of microstructure was also accounted in this study. Qin et al. [20] reported tensile and compressive properties in 3D porous graphene architectures, where the porous network was obtained by introducing spherical inclusions in a sea of dispersed graphene flakes. They proposed using

* Corresponding author at: Department of Mechanics of Solids, Surfaces & Systems, University of Twente, PO Box 217, Enschede, 7500 AE, The Netherlands.
E-mail address: ameya.rege@utwente.nl (A. Rege).
URL: https://people.utwente.nl/ameya.rege (A. Rege).

https://doi.org/10.1016/j.commatsci.2026.114909
Received 26 February 2026; Received in revised form 9 June 2026; Accepted 9 June 2026

the AIREBO force field to model the internal interactions among carbon atoms in graphene. Inspired by this study, Patil et al. [21] reported on the fracture mechanics of similarly generated porous graphene networks terming them graphene aerogels. Fracture properties such as fracture strength and fracture toughness were reported. The power-law dependency of the elastic modulus and the tensile strength on density was demonstrated. Recently, similar study focusing on the mechanistic response using all atom simulations have been extended to investigate the amorphous carbon systems revealing that the strength of such systems is mainly attributed to the presence of sp^3 carbon atoms [22,23]. Yu et al. [24] reported the elastic properties and plastic deformation, at an atomistic level, of nanoporous amorphous carbon using machine learning-driven simulations. One can observed, amorphous carbon as well as graphene, including porous graphene, has been well investigated for their mechanical and fracture properties using MD. To the best of the knowledge of the authors, there have not been many reports on the mechanical and fracture behaviour of nanostructured porous carbon. Experimental studies on macroscopic mechanical behaviour and failure of nanoporous carbon (carbon aerogels) have been reported [10]. Compression tests and three point bending tests were performed to quantify the mechanical properties of various types of carbon aerogels. Morphological changes under deformation were investigated using digital correlation image studies and in-situ SEM measurements. However, the bottleneck still lies in investigating the properties of porous carbon structures at a molecular level. To this end, we build up on our previous model [25] and investigate the mechanical and fracture behaviour of nanostructured porous carbon.

In this work, we report on the cyclic deformation under compression and fracture behaviour under tension of nanoporous carbon using an all-atom MD modelling approach. The objective was to study the damage and residual deformation under cyclic deformation in such porous carbons as well as crack propagation mechanism subject to existing notches at the molecular level. Fracture toughness and elastic modulus were evaluated for nanoporous carbon by employing notched specimens with varying notch length-to-height ratios. Samples with different densities were analysed to assess how these properties depend on the solid fraction. For each structure, multiple notch lengths were introduced to examine the influence of crack size on the tensile deformation response.

The paper is structured as follows. The Materials and Methods section first details the modelling framework used to generate the porous carbon structures, followed by a description of the mechanical simulation setup employed to characterise the tensile, compressive, and fracture behaviour of nanoporous carbon. The Results section presents the findings from tensile fracture simulations, after which the response under compressive loading is discussed together with a validation of the results. Finally, the paper concludes with a summary of the key outcomes and an outlook on potential directions for future research building on this work.

2. Materials and methods

The model development and all simulations of the mechanical and fracture properties of nanostructured porous carbon networks were carried out using Large scale Atomic/Molecular Massively Parallel Simulator (LAMMPS) [26]. The Adaptive Intermolecular Reactive Empirical Bond Order (AIREBO) potential was found to be a suitable choice for a force field, given that it accounts for the long-range, short-range, and dihedral interactions and has been previously reported to accurately describe purely carbon-based materials [20,21,27,28]. The force-field is expressed by the equation,

$$E = \frac{1}{2}\sum_{i}\sum_{j\neq i}\left[E_{ij}^{REBO} + E_{ij}^{LJ} + \sum_{k\neq i,j}\sum_{l\neq i,j,k} E_{kijl}^{TORSION}\right], \quad (1)$$

where the E^{REBO} term gives the model its reactive capabilities and describes short-ranged C–C interactions ($r < 2$Å). These interactions have strong coordination-dependence through a bond order parameter, which adjusts the attraction between the i, j atoms based on the position of other nearby atoms and, thus, has three- and four-body dependence [28]. The E^{LJ} term adds longer-ranged interactions ($2 < r <$ cutoff) using a form similar to the standard Lennard-Jones (LJ) potential. It contains a series of switching functions so that the short-ranged LJ repulsion ($1/r^{12}$) does not interfere with the energetics captured by the E^{REBO} term. The extent of E^{LJ} interactions is determined by the cutoff argument to the pair style command which is a scale factor. A cutoff radius of 2.5 Å was employed to model the interatomic interactions and was chosen to ensure accurate representation of short-range covalent interactions while avoiding artificial long-range bonding, which is critical for simulating bond breaking and structural evolution in porous carbon under mechanical loading. This cutoff value is widely adopted in MD simulations of carbon-based systems, including porous and disordered carbon structures, and has been shown to accurately capture covalent bonding and mechanical response under deformation. Previous studies on carbon honeycomb and related porous carbon systems have also used the same cutoff value, ensuring consistency with established literature [29,30]. The $E^{TORSION}$ is the four-body term that describes various dihedral angle preferences in hydrocarbon configurations.

2.1. Carbon model development

The carbon models were developed using the methodology described in our previous work [25]. Briefly, as a first step, 800000 carbon atoms were initialised and randomly distributed in a simulation box of 30 nm. This system has a density of 0.591 g cm^{-3}. This highly disordered system is equilibrated for 25 ps under constant-temperature and constant-pressure (NPT) conditions. An amorphous carbon structure is obtained by subjecting the system to a high temperature of 5000 K for 25 ps and kept at this high temperature for 25 ps before being cooled back to 300 K at constant-temperature and constant-volume (NVT) conditions and equilibrated for 25 ps at NPT conditions. The resulting structure is then allowed to relax under stable pressure conditions. At this point, the formation of an initial structure of a clustered network of carbon is observed. This initially formed network of voids and clusters serves as a starting point for the formation of micro- and mesopores. On instantaneous expansion and subsequent NPT–NVT equilibration cycles, structures with lower and desired densities can be obtained. It is worth noting that the equilibration plays a major role in allowing the atoms to regain the most energetically favourable positions. At lower densities, with higher expansion, higher NVT equilibration times are required. Once the MD models of nanoporous carbon are completely simulated, their visualisation is done using OVITO [31]. The atomistic models with densities of $0.591, 0.269, 0.144$ g cm^{-3} were constructed and subsequently employed to investigate the mechanical and fracture properties in this study. Since the nanostructured porous carbon geometries are stochastically generated, three independent realisations were used per density to ensure statistical robustness.

2.2. Simulation of the mechanical and fracture properties

To study the mechanical properties of the carbon models, periodic boundary conditions were employed on the generated representative volume elements (RVEs) with a box-size of 30 nm x 30 nm x 30 nm. First, since the study was aimed at understanding the quasistatic behaviour of porous carbons, the strain-rate sensitivity analysis was conducted to eliminate any influence of the strain-rate on the resulting mechanical behaviour. To quantify this effect, the Young modulus of the porous carbon model of density 0.591 g cm^{-3} was determined at different strain rates: 0.4, 0.04, 0.004 and 0.0004 ps^{-1}. The model structures were deformed using a time-step size of 0.5 fs and using an NPT ensemble under atmospheric conditions. The elastic modulus was determined from the slope of the linear region at infinitesimal strains.

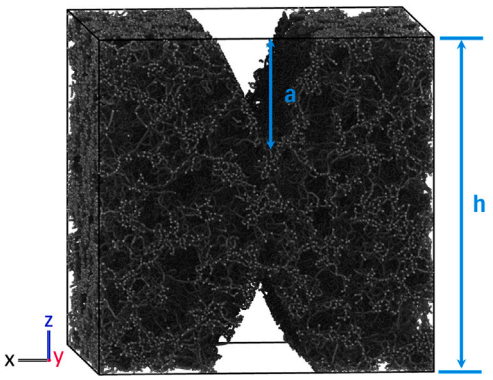

Fig. 1. Schematic representation of all atom porous carbon model of density 0.591 g cm^{-3} for calculation of crack depth to height ratio.

The optimum strain rate was determined and used for subsequent simulations.

Uniaxial tension up to fracture and uniaxial compression with loading–unloading cycles with increasing maximal strain were also performed on the so-generated RVEs. To undertake in-depth investigation on the fracture behaviour, models with v-shaped notches were introduced onto the structures by removing atoms as shown in Fig. 1. These double notched systems were built using OVITO. The periodic vector through the y axis was considered, resulting in fracture models of infinite length along y-direction. The atomic structure was then relaxed up to 100 ps using the NVT ensemble. For a heuristic analysis, the depth of the notch was varied for each density type of the nanostructured porous carbon structure.

In general, tensile loading is applied perpendicular to the crack plane to study the fracture toughness.

2.2.1. Fracture theory

The fracture behaviour of brittle solids can be studied within the framework of linear elastic fracture mechanics (LEFM) [32]. Griffith postulated that crack propagation in an elastic material occurs when the reduction in stored elastic strain energy due to crack propagation compensates for the energy required to create new free surfaces. In other words, a crack becomes unstable when the energy for crack growth equals or exceeds the material's surface energy resulting in crack propagation. Based on this, the fracture strength of a body in which a crack has been introduced can be expressed as:

$$\sigma_f = \sqrt{\frac{2E\gamma_s}{\pi a}}, \tag{2}$$

where σ_f denotes the critical stress at fracture or referred to here as fracture strength, E is the elastic modulus, γ_s is the surface energy, and a denotes the crack depth.

E was calculated within the linear segment of the stress–strain curve obtained from the uniaxial tensile deformation of the material, generally applied perpendicular to the crack plane.

For specimens of finite dimensions, geometric effects influence the stress distribution near the crack tip. To account for these finite-size and geometrical corrections, a dimensionless factor α is introduced, leading to the modified expression

$$\sigma_f = \frac{1}{\alpha}\sqrt{\frac{2E\gamma_s}{\pi a}}, \tag{3}$$

where α is a geometric correction factor that accounts for finite-size effects and mainly depends upon specimen geometry and crack configuration. The specimens studied here are double-edge notched with varying a and h as visualised in Fig. 1 and hence, appropriate calculations for geometric corrections need to be considered. Based on the theory of fracture mechanics by Nestor Perez [33], in the specific case of a double-edge notched specimen of semi-infinite width with crack height h, the factor α can be expressed as

$$\alpha = 1.12 + 0.43\left(\frac{a}{h}\right) - 4.79\left(\frac{a}{h}\right)^2 + 15.46\left(\frac{a}{h}\right)^3. \tag{4}$$

An alternate description of brittle fracture was later formulated by Irwin [34], who introduced the concept of the strain energy release rate, G. Irwin modified Griffith's theory by recognising that crack propagation is governed by the total energy required for fracture, which includes not only surface energy γ_s but also additional dissipative processes such as plastic deformation. He introduced G and stress intensity factor K formulations to account for these effects in real materials. The parameter G represents the amount of elastic energy released per unit increment of crack surface area. For a linear elastic solid, the energy release rate can be related to the applied stress and crack size as

$$G = \frac{\alpha^2\sigma_f^2\pi a}{E}. \tag{5}$$

Fracture initiation occurs when this energy release rate reaches a critical value, G_C, characteristic of the material. Irwin also defined K, which characterises the amplitude of the stress field near the crack tip. The critical value, K_{IC}, commonly referred to as the fracture toughness, quantifies the material's resistance to crack propagation. Unlike fracture strength, both G_C and K_{IC} are intrinsic material properties. The relationship between the critical stress intensity factor, the fracture strength, and the energy release rate is expressed as

$$K_{IC} = \alpha\sigma_f\sqrt{\pi a} = \sqrt{G_C E}. \tag{6}$$

These formulations collectively provide the theoretical foundation for evaluating fracture strength and toughness in brittle materials within the framework of linear elastic fracture mechanics. In this work, σ_f is obtained from the tensile deformation curves. The point of maximum stress after which the system ruptures is defined as the fracture strength of the system. Elastic modulus is calculated from the linear elastic region for each system. Hence, by using the Eqs. 5 and 6, the strain energy release rate G_C and fracture toughness K_{IC} were calculated.

It should be noted, however, that the present material consists of a discrete nanoporous carbon network rather than a homogeneous continuum. Consequently, the assumptions underlying classical Griffith theory and LEFM are only approximately satisfied, particularly when the crack size becomes comparable to the characteristic microstructural length scale of the network. Therefore, the calculated values of K_{IC} and G_C should be interpreted as effective fracture descriptors obtained within a continuum approximation. These parameters provide a useful quantitative measure of the apparent fracture resistance of the nanoporous network and enable systematic comparison between different crack sizes and network morphologies. However, they should not necessarily be regarded as intrinsic material properties that are independent of geometry, flaw size, or microstructural features. As the crack length becomes reasonably larger than the characteristic ligament and pore dimensions, the continuum approximation is expected to become increasingly valid, and the extracted fracture parameters approach their classical LEFM interpretation.

3. Results and discussion

To study the mechanical and fracture properties of nanostructured porous carbon under quasistatic conditions, it was imperative to conduct a parameter sensitivity analysis for the effect of strain rate [35–38]. This was evaluated by calculating the value of elastic modulus E, by subjecting the system to tensile deformation at various strain rates. Fig. 2(b) shows the variation of elastic modulus with respect to the change in applied strain rate. The modulus is sensitive to strain rate at higher values. Beyond a strain rate of 0.004 ps^{-1}, E does not seem to be affected, and therefore this was chosen as an optimum value for all subsequent simulations.

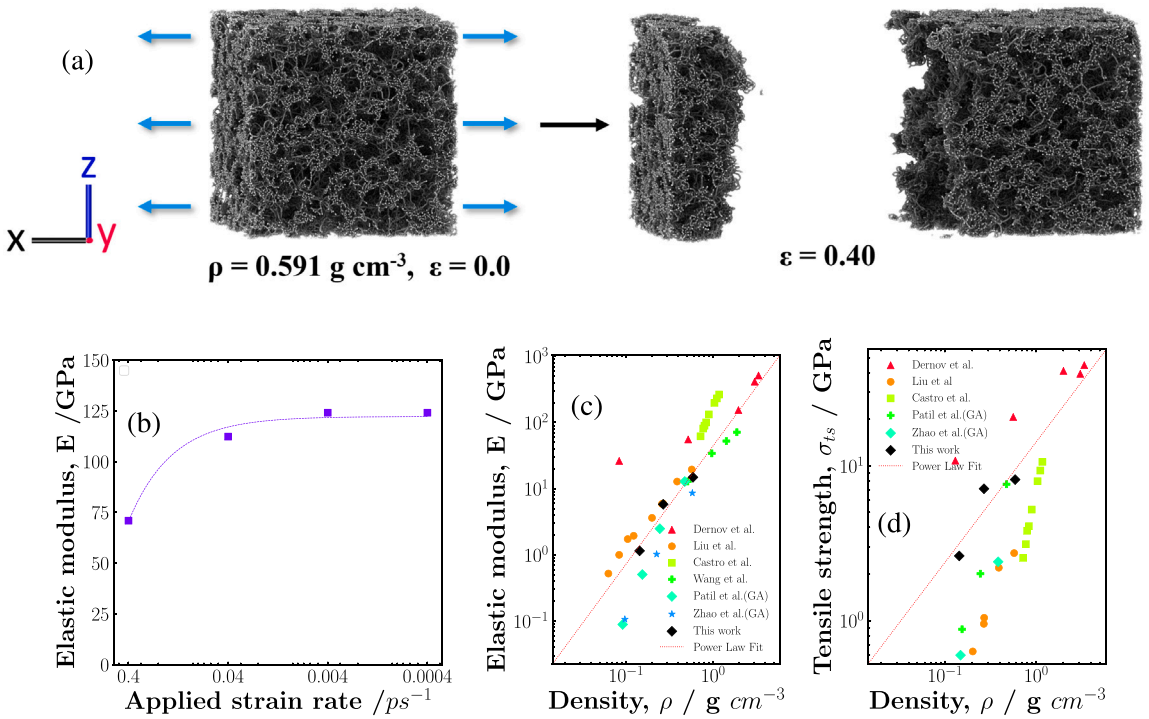

Fig. 2. (a) Nanoporous carbon of density $\rho = 0.591$ g cm^{-3} subjected to tensile deformation up to fracture, where complete fracture occurs at $\varepsilon = 0.4$. (b) Influence of strain rate on the elastic modulus of nanoporous carbon with density 0.591 g cm^{-3}. (c) Elastic modulus, E versus density, ρ of porous carbon structures under tensile deformation compared to the literature values. (d)Tensile strength, σ_{ts} versus density, ρ of porous carbon structures under tensile deformation compared to the literature values.

3.1. Uniaxial tension

As discussed earlier, models of varying densities are developed in order to study mechanical properties of porous carbon. The models at densities of $0.591, 0.269, 0.144$ g cm^{-3} were subjected to tensile loading until complete rupture as demonstrated in Fig. 2(a). The elastic modulus was calculated within 5% of the applied strain and the peak stress the notched system undergoes before fracture is considered as the fracture strength. Figs. 2(c) and (d) show the elastic modulus, E, and tensile strength, σ_{ts}, respectively, of the modelled nanoporous carbon systems as functions of density, ρ. The results are also supported by data from the literature [20–23,39,40]. A power law relation between E and ρ was fitted for the data from this work and the obtained power law exponent was 1.79 ± 0.05 which is in agreement with the literature works [39,40]. This trend is further corroborated by the data shown in Fig. 2(c). The obtained exponent lies between 1 and 2, but is closer to 2, indicating a predominantly bending-dominated deformation mechanism, in line with the Gibson–Ashby model. This exponent shows deviation from the one calculated from compression-derived modulus [25]. This suggests strong tension–compression asymmetry and originates from differences in the underlying deformation mechanisms that are already active at small strains. In compression, the response is influenced by bending-dominated kinematics, non-affine deformation, and sensitivity to incipient structural instabilities, whereas tension promotes more affine deformation and greater participation of axial stretching in load-bearing ligaments. These differences in the relative contributions of bending and stretching lead to distinct stiffness–density scaling behaviour, even within the nominally linear regime. The power-law fit for tensile strength in Fig. 2(d) agrees well with the data for amorphous carbon but slightly deviates from the trends of graphene aerogels. This shows that while the Young's modulus scales similarly for porous carbon and graphene materials, the tensile strength scales differently. With increasing density, the tensile strength increases, but the failure strain decreases. This is consistent with the observations of

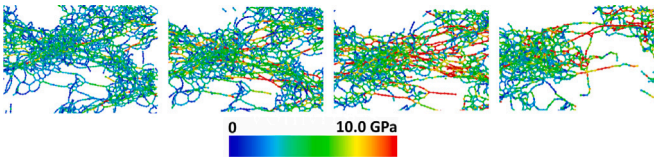

Fig. 3. Evolution of local stress contours during uniaxial tensile loading up to fracture for model with a density of 0.591 g cm^{-3}.

Liu et al. and Patil et al. [21,39] for graphene aerogels, as well as reports on other nanostructured porous systems [41,42]. At a higher density of 0.591 g cm^{-3}, the drop in tensile stress, σ_t due to increasing strain is more sharp which can demonstrate that the maximum number of bond-breaking took place within a very short strain step. However, for low density structure, we see that the failure does not occur instantaneously. This can be attributed to the larger voids and higher possibilities of molecular rearrangements before undergoing full fracture. The low density structures, at a molecular level, undergo large strains before fracture. Yu et al. [24] have reported that the tensile properties are directly related to the pore sizes and the pore-size distribution of nanoporous carbon. There, it was shown that the nanoporous alpha carbon structures exhibited yielding at volumetric strain of 21%, beyond which the stress drops as the volumetric strain increases and plastic deformation mechanisms are activated [23,24]. They also report that the strain required for the nanoporous amorphous carbon to yield is inversely proportional to their density.

The structural changes occurring during stretching, as observed in Fig. 3, reveal that small and medium sized rings with higher strain at the points of fracture get deformed and rearrange themselves into sp^2 configurations and on further tensile stretching into sp configuration as seen by formation of long chains before final fracture. In the developed models, sp^3 configurations exhibit a significantly lower percentage compared to sp and sp^2 configurations. There is a relative reduction

in sp^3 coordination accompanied by an increase in sp^2 and sp configurations only until fracture, indicating bond dissociation and structural rearrangement during fracture. Beyond the fracture point, the system undergoes structural relaxation to attain a lower energy state, seen as small increase in sp^2 configurations across all density cases and the stabilisation of sp configurations. The six member rings are comparatively more stable towards the tensile stretching. Similar mapping of structural changes were previously observed by Dernov et al. [23]. Another notable characteristic during tensile loading is the evolution of microstructure with respect to the stress concentrations as seen in Fig. 3. Tensile deformation initiates localised stress concentrations within the ligament regions, which undergo progressive narrowing with increasing strain. This structural evolution from densely interconnected networks to isolated single chain configurations at critical failure points exposes the underlying microscopic mechanisms of deformation and fracture under uniaxial loading. To investigate this, snapshots of atomistic configuration at the site of rupture was taken into consideration. It was observed that these atoms experience elevated stress during rupture. With an increase in strain, five and seven membered rings undergo faster reconfiguration and eventually fracture compared to six membered rings as they have uneven stress distributions due to their geometric instability. As the strain increases, the ring structures reconfigured to form sp chains which is further subjected to high enough stress concentration eventually causing rupture.

3.2. Fracture behaviour

To investigate the influence of pre-existing defects on crack propagation, v-shaped notches were introduced into the modelled porous carbon structures. The effect of crack size was examined by systematically varying the crack length-to-height ratio, a/h. Models with different a/h values were then subjected to uniaxial tensile loading along the x-axis, during which they underwent progressive elongation prior to complete fracture. The stress corresponding to final failure was defined as the fracture strength. An exemplary illustration of the crack propagation process leading to complete fracture is provided in Fig. 4. At a density of 0.591 g cm^{-3}, the complete fracture occurs at a strain of 0.497 for an a/h value of 0.03.

As shown in Fig. 5(a), tensile loading introduces significant changes in the microstructure. The figure illustrates a zoomed snapshot of the site of rupture under tensile loading. The evolution of strain reveals the underlying microscopic deformation mechanisms and the fracture patterns that develop during tensile stress. In particular, the clustered carbon network comprising five-, six-, and seven-membered rings undergoes progressive bond breakage. Fracture is initiated in regions or clusters characterised by inherent geometric instabilities, which can be interpreted as zones of elevated stress concentration. As the strain increases, σ-bonds associated with sp^2-hybridised carbon atoms transiently reorganise into chain-like structures before ultimately rupturing. These observations are consistent with observations by Yu et al. [24].

Fig. 5(b) shows the subsequent σ_t - ε_t curves along the loading direction with varying a/h values for the structure with a density of 0.591 g cm^{-3}. It is observed that the response for all cases is largely linear up to σ_f. Also, the response softens with increasing a/h ratios. For a small a/h of 0.03, the fracture strength is as high as 7.47 GPa while for larger values, e.g., a/h=0.3, the stress value decreases to 3.47 GPa. Fig. 5(c) demonstrates the effect of a/h on σ_f for the simulated models with densities of 0.591, 0.269, 0.144 g cm^{-3}. It can be observed that the overall fracture strength of the structures decreases with increasing a/h ratio. In parallel, it also decreases with decrease in the density. The model with lowest density 0.144 shows some irregularities in σ_f at $a/h < 0.05$ while showing steady decrease in σ_f at $a/h > 0.05$. This could be attributed to the structure of porous carbon at lower densities, which has less graphitic rings and can undergo more molecular rearrangement during crack formation and equilibration. Further description of the structural and geometric features of porous carbons is given in our previous work [25]. The relationship between elastic modulus, E and a/h for different densities is also illustrated in Fig. 5(d). The value of E is in general higher for higher densities and shows more or less linearly decreasing trend with respect to increasing a/h. For the lowest density samples, the decrease is negligible. The values of E and σ_f are further utilised to calculate the fracture toughness, K_{IC} and elastic strain energy at crack, G_C using the Griffith's criterion as described in Eq. (2).

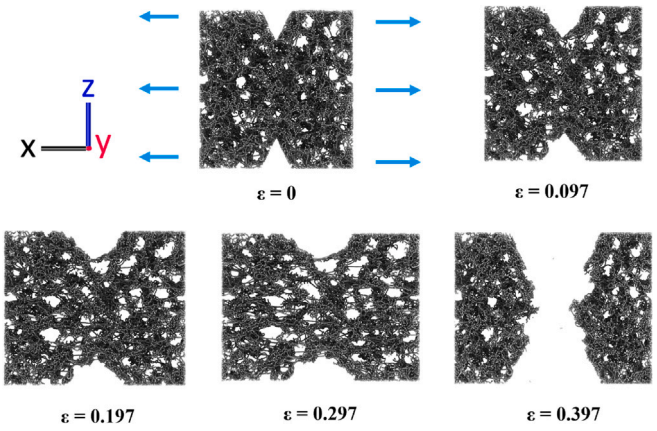

Fig. 4. Deformation snapshots of density 0.591 g cm^{-3} with crack depth to height ratio, a/h = 0.2 until fracture. The arrows in the initial snapshot represents the direction of tensile stress applied.

Fig. 5(e) shows the relationship between fracture toughness, K_{IC} and a/h for the investigated densities. One could observe that samples with higher densities exhibit a higher K_{IC} which is in line with the trends seen for σ_f and E. Also, at a low density of 0.144 g cm^{-3}, the K_{IC} remains mostly unaffected by a/h and is in the range of 0.2–0.3 MPa m$^{1/2}$. At higher densities, a general trend of increasing K_{IC} is seen with respect to a/h, with observable increments before reaching a plateau. For the models with densities of 0.591 g cm^{-3} and 0.269 g cm^{-3}, the fracture toughness values were found to converge when $a/h >= 0.1$, indicating that further increases in crack length do not significantly affect the measured toughness.

Fig. 5(f) illustrates the relationship between the critical strain energy release rate, G_C and a/h. G_C at the lowest density of 0.144 g cm^{-3} exhibits minimal sensitivity to variations in a/h. For most a/h ratios, G_C remains within the range of 40–45 J m^{-2}. The only notable deviation occurs at a/h = 0.03, where a substantially reduced value of 26 J m^{-2} was observed. At higher densities of 0.591 and 0.269 g cm^{-3}, a general trend of increasing G_C is seen with respect to a/h, before reaching a plateau. For the model with the highest density of 0.591 g cm^{-3}, the G_C values were found to converge when $a/h >= 0.15$, indicating that further increases in crack length do not significantly affect G_C. For the model with the density of 0.269 g cm^{-3}, the G_C values were found to converge when $a/h >= 0.05$. This phenomena of higher G_C values for lower densities matches well with the trends shown for silica aerogels [43].

A larger a/h ratio corresponds to a longer crack relative to the specimen height, which increases the stress intensity factor for a given applied stress. As a result, fracture is initiated at lower applied stresses with increasing crack length. While the intrinsic fracture toughness remains independent of crack size under ideal linear elastic fracture mechanics conditions, the observed response reflects a transition in deformation mechanisms. For small a/h, a larger fraction of the material participates in deformation, leading to significant bond stretching, pore collapse, and enhanced energy dissipation prior to fracture. In contrast, for large a/h, deformation becomes highly localised near the crack tip, promoting rapid crack propagation with limited bulk deformation and reduced overall energy dissipation.

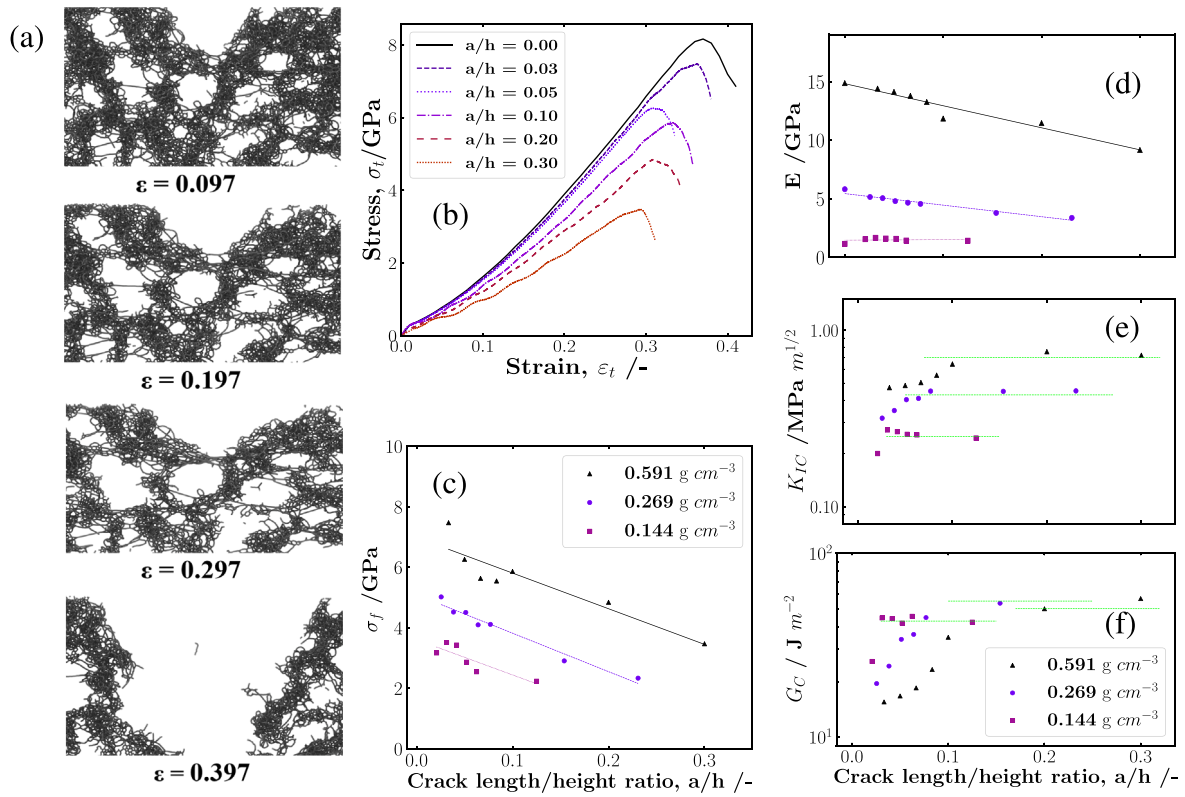

Fig. 5. (a) Snapshots of notched structure of porous carbon of density 0.591 g cm^{-3} with a a/h of 0.1, taken at various strain levels, ε = 0.097, 0.197, 0.297 and 0.397. (b) Stress–strain curves of porous carbon with a density of 0.591 g cm^{-3} with crack depth to height ratio, a/h varying between 0.03 to 0.3. (c) Fracture strength of porous carbon structures at varied notch depths, calculated as the highest stress the material undergoes before fracture. (d) Elastic modulus versus the crack length to height ratio for porous carbon with varied densities. (e) Effect of notch depth on the fracture toughness of the porous carbon structures with varying densities. (f) Influence of crack length to height ratio on the strain energy release rate of the porous carbon structures.

The above-illustrated results provide a mechanistic framework for designing mechanically resilient porous carbon electrodes for metal-sulphur batteries, which are repeatedly subjected to chemo-mechanically induced stresses during cycling. The observed density dependence reveals a fundamental trade-off: Higher-density nanoporous carbons exhibit greater stiffness and tensile strength but fail more abruptly with lower failure strain, indicating a more brittle and flaw-sensitive response, whereas lower-density networks accommodate significantly larger strains through molecular rearrangements before complete rupture. This distinction is highly relevant for electrodes that experience cyclic expansion and contraction due to sulphur conversion reactions, where abrupt fracture can lead to rapid loss of electronic percolation and mechanical integrity. The notch-sensitivity study further demonstrates that fracture strength decreases systematically with increasing defect size (a/h), particularly at higher densities, underscoring the critical role of flaw population and processing-induced defects in determining electrode durability. In contrast, the relative insensitivity of fracture toughness and strain energy release rate to crack size at lower densities suggests a more damage-tolerant architecture capable of redistributing stresses rather than localising them catastrophically. At the atomic scale, the observed transient bond reorganisation and chain formation prior to rupture point towards intrinsic nanoscale toughening mechanisms that may delay crack propagation under cyclic loading. Collectively, these findings indicate that optimising porous carbon electrodes for metal–sulphur batteries requires not only maximising strength, but carefully balancing density, defect tolerance, and energy dissipation capacity to preserve structural integrity and electrical connectivity over prolonged electrochemical cycling.

3.3. Uniaxial compression

The developed porous carbon models were subjected to uniaxial compression. The effect of density on their constitutive behaviour under uniaxial compression was studied as demonstrated in Fig. 6(a). A J-shaped behaviour is observed with no visible plateau. This can be a result of rapid pore collapse resulting in a quick initiation of densification. Models with densities of 0.269 g cm^{-3} and 0.144 g cm^{-3} exhibit a more gradual pore collapse. For the model with a density of 0.591 g cm^{-3}, a steep rise in compressive stress at high strain values beyond 0.2 is observed, indicating classical densification upon pore collapse. In contrast, lower density structures do not undergo complete pore collapse at the applied strains. Similar observations have been reported for other nanostructured porous materials [20,21,44].

Under uniaxial compressive loading, progressive pore collapse is evident from the spatial distribution of stress concentrations. These results are an extension of our previous study revealing pore collapse during compression of nanoporous carbon networks [25]. In the case of high density structure 0.591 g cm^{-3}, sp^2 configuration also decrease with increasing compressive stress indicating higher densification which is consistent with the quantitative studies showing higher elastic modulus.

3.4. Cyclic deformation

The porous carbon structures were subjected to incremental uniaxial compression up to prescribed maximal strain levels ranging from 0.05 to 0.39, followed by unloading to zero stress, as illustrated in Fig. 6(b). The σ_c - ε_c was obtained from six consecutive loading and unloading cycles. The observed cyclic stress–strain curves of porous carbon models

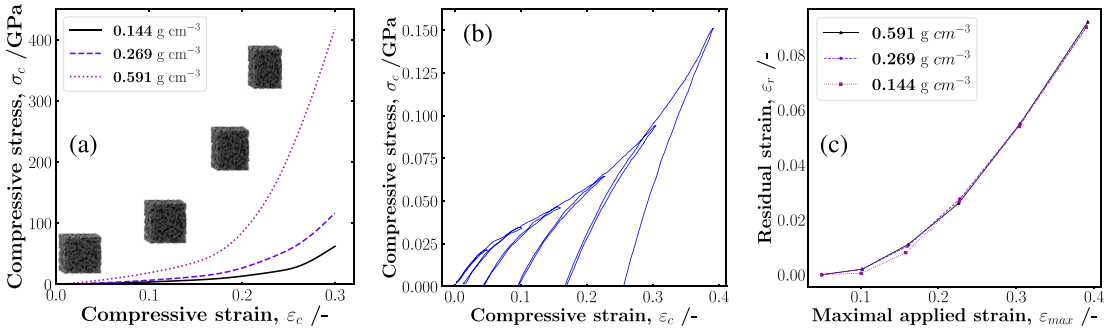

Fig. 6. (a) Comparison of compressive stress–strain curves of porous carbon structures at different densities. (b) Stress–strain curve of cyclic compressive loading of porous carbon with a density of 0.591 g cm^{-3}. (c) Residual strain versus the maximum compressive strain applied on porous carbon structures.

demonstrate a damage-induced softening effect, where initial loading cycle shows significantly higher stiffness compared to subsequent cycles. These effects are similar to the ones reported in literature [45]. Under such a cyclic loading–unloading scenario, significant residual deformation and hysteresis was observed. With an increase in the applied maximal strain, ε_{max}, an increase in the residual strain, ε_r was observed. This indicates irreversible deformation in the material. Fig. 6(c) shows the increment of ε_r in the material with respect to ε_{max}. It is interesting to observe that the values of residual strain coincides for all densities and grows similarly with the maximal applied strain.

The results from compression of the nanoporous carbon networks provides important insight into their suitability as mechanically resilient hosts in metal-sulphur batteries, where electrodes are continuously subjected to stack pressure, calendaring-induced pre-compression, and chemo-mechanical expansion during cycling. The observed J-shaped stress–strain response without a distinct plateau indicates rapid pore collapse and early densification, particularly for the higher-density structure, which shows a steep stress increase beyond about 0.2 strain. This suggests that dense networks quickly transition from a compliant porous scaffold to a compacted load-bearing skeleton, a feature that may enhance electrical contact and structural integrity under pressure, but at the cost of increased stress concentration once densification initiates. In contrast, the lower-density architectures exhibit more gradual pore collapse and avoid complete densification within the applied strain range, providing a broader mechanical buffer to accommodate cyclic volume changes without abrupt stiffening. The cyclic compression results further strengthen this interpretation: The pronounced stress softening after the first loading cycle, together with hysteresis and increasing residual strain, reveals a damage-induced conditioning process reminiscent of Mullins-type behaviour, where irreversible microstructural rearrangements and partial pore collapse progressively alter the mechanical response. Importantly, the residual strain scales primarily with the applied maximal strain rather than density, indicating that peak compressive strain-rather than density alone govern irreversible compaction. For metal-sulphur electrodes, this implies that mechanical durability depends not only on selecting a sufficiently strong carbon scaffold, as highlighted by the tensile and fracture analyses, but on designing architectures that avoid repeated entry into the densification regime while still maintaining percolating electrical pathways. Balancing density, compliance, and resistance to irreversible compaction therefore emerges as a central strategy for sustaining structural integrity and electrochemical performance over long-term cycling. This opens up diverse areas for further investigations on mechanics of nanostructured porous carbon along the lines of long-term cyclic compression.

4. Conclusion

In this work, the tensile, fracture, and cyclic compressive behaviour of nanostructured porous carbons were systematically investigated using all-atom molecular dynamics simulations. Under uniaxial tension, the porous carbon frameworks exhibited linear elastic behaviour up to the fracture strength, beyond which structural failure occurred due to progressive bond breaking within the carbon network. The calculated fracture toughness K_{IC} and critical energy release rate G_C demonstrated a clear dependence on material density for smaller cracks and exhibited convergence beyond a crack length-to-height ratio $a/h \approx 0.1$, indicating the existence of a characteristic defect size beyond which fracture properties become geometry-insensitive. Higher-density structures showed increased stiffness, strength, and toughness, whereas lower-density networks displayed enhanced deformability and more progressive failure mechanisms, reflecting the strong influence of architecture on mechanical performance.

The compressive response further revealed pronounced density-dependent behaviour, characterised by a J-shaped stress–strain curve associated with rapid pore collapse and the onset of densification. High-density models exhibited early stiffening at larger strains, while lower-density systems accommodated deformation more gradually without complete pore collapse within the investigated strain range. Cyclic compression tests highlighted significant hysteresis and residual strain accumulation, providing evidence for irreversible microstructural rearrangements and damage-induced softening. Notably, the residual strain evolution was governed primarily by the maximal applied strain rather than density, underscoring the critical role of maximum deformation levels experienced during loading in determining long-term structural integrity. A pronounced tension–compression asymmetry was observed, arising from differences in deformation kinematics, with tension favouring stretching-dominated response and compression being governed by bending and instability-driven mechanisms.

While experimental studies on carbon aerogels predominantly report bulk mechanical properties, they often lack insight into particle-level and microstructural deformation mechanisms that ultimately govern electrochemical reliability. The present atomistic simulations address this gap by resolving deformation and fracture processes at the molecular scale. Although the simulated systems were subjected to uniaxial strains up to approximately 30%, experimentally synthesised flexible carbon aerogels typically exhibit pore sizes in the mesoporous regime (2–50 nm), as well as macropores (larger than 50 nm), where flexibility is strongly influenced by pore architecture. The demonstrated structural stability of the modelled nanoporous carbons up to 20% deformation indicates substantial intrinsic resistance to mechanical stresses at the atomic level, suggesting that the fundamental carbon framework can sustain significant strain before catastrophic failure.

CRediT authorship contribution statement

Hemangi Patel: Writing – original draft, Visualization, Validation, Software, Methodology, Investigation, Formal analysis, Data curation. **Barbara Milow:** Writing – review & editing, Supervision. **Ameya Rege:** Writing – review & editing, Supervision, Formal analysis, Conceptualization.

Declaration of competing interest

The authors declare that they have no known competing financial interests or personal relationships that could have appeared to influence the work reported in this paper.

Acknowledgements

The authors gratefully thank the Regionales Rechenzentrum der Universität zu Köln (RRZK) for providing the computing time on the Research Accelerator for Modeling and Simulation with Enhanced Security (RAMSES) at the University of Cologne.

Data availability

Data will be made available on request.

References

[1] J. Biener, M. Stadermann, M. Suss, M.A. Worsley, M.M. Biener, K.A. Rose, T.F. Baumann, Advanced carbon aerogels for energy applications, Energy & Environ. Sci. 4 (3) (2011) 656–667.
[2] M. Nojabaee, B. Sievert, M. Schwan, J. Schettler, F. Warth, N. Wagner, B. Milow, K.A. Friedrich, Ultramicroporous carbon aerogels encapsulating sulfur as the cathode for lithium-sulfur batteries, J. Mater. Chem. A 9 (10) (2021) 6508–6519.
[3] A. Smirnova, X. Dong, H. Hara, A. Vasiliev, N. Sammes, Novel carbon aerogel-supported catalysts for PEM fuel cell application, Int. J. Hydrog. Energy 30 (2) (2005) 149–158.
[4] B. Ding, C. Yuan, L. Shen, G. Xu, P. Nie, X. Zhang, Encapsulating sulfur into hierarchically ordered porous carbon as a high-performance cathode for lithium–sulfur batteries, Chem. : A Eur. J. 19 (3) (2013) 1013–1019.
[5] A. Fu, C. Wang, F. Pei, J. Cui, X. Fang, N. Zheng, Recent advances in hollow porous carbon materials for lithium-sulfur batteries, Small 15 (10) (2019) 1804786.
[6] R.W. Pekala, C.T. Alviso, Carbon aerogels and xerogels, MRS Online Proc. Libr. 270 (1) (1992) 3–14.
[7] R. Saliger, V. Bock, R. Petricevic, T. Tillotson, S. Geis, J. Fricke, Carbon aerogels from dilute catalysis of resorcinol with formaldehyde, J. Non-Cryst. Solids 221 (2) (1997) 144–150.
[8] M. Schwan, L. Ratke, Flexible carbon aerogels, C – J. Carbon Res. 2 (3) (2016) 22.
[9] M. Antonietti, N. Fechler, T.-P. Fellinger, Carbon aerogels and monoliths: control of porosity and nanoarchitecture via sol-gel routes, Chem. Mater. 26 (1) (2014) 196–210.
[10] A. Rege, M. Schwan, L. Chernova, M. Hillgärtner, M. Itskov, B. Milow, Microstructural and mechanical characterization of carbon aerogels: an in-situ and digital image correlation-based study, J. Non-Cryst. Solids 529 (2020) 119568.
[11] J. Kröner, D. Platzer, B. Milow, M. Schwan, Electrical conductivity of monolithic and powdered carbon aerogels and their composites, Mater. Adv. 5 (20) (2024) 8042–8052.
[12] W.T. Ashurst, W.G. Hoover, Microscopic fracture studies in the two-dimensional triangular lattice, Phys. Rev. B 14 (4) (1976) 1465–1473.
[13] B. De Celis, Molecular Dynamics Simulation Studies in Fracture Mechanics (Ph.D. thesis), 1982.
[14] F.F. Abraham, D. Brodbeck, W.E. Rudge, X. Xu, A molecular dynamics investigation of rapid fracture mechanics, J. Mech. Phys. Solids 45 (9) (1997) 1595–1619.
[15] J. Swadener, M. Baskes, M. Nastasi, Molecular dynamics simulation of brittle fracture in silicon, Phys. Rev. Lett. 89 (8) (2002) 085503.
[16] S.C. Chowdhury, E.A. Wise, R. Ganesh, J.W. Gillespie Jr., Effects of surface crack on the mechanical properties of Silica: A molecular dynamics simulation study, Eng. Fract. Mech. 207 (2019) 99–108.
[17] A.E. Mayer, P.N. Mayer, Evolution of pore ensemble in solid and molten aluminum under dynamic tensile fracture: Molecular dynamics simulations and mechanical models, Int. J. Mech. Sci. 157 (2019) 816–832.
[18] K. Mylvaganam, L. Zhang, Important issues in a molecular dynamics simulation for characterising the mechanical properties of carbon nanotubes, Carbon 42 (10) (2004) 2025–2032.
[19] P.-Y. Yang, S.-P. Ju, S.-M. Huang, Predicted structural and mechanical properties of activated carbon by molecular simulation, Comput. Mater. Sci. 143 (2018) 43–54.
[20] Z. Qin, G.S. Jung, M.J. Kang, M.J. Buehler, The mechanics and design of a lightweight three-dimensional graphene assembly, Sci. Adv. 3 (1) (2017) e1601536.
[21] S.P. Patil, P. Shendye, B. Markert, Molecular investigation of mechanical properties and fracture behavior of graphene aerogel, J. Phys. Chem. B 124 (28) (2020) 6132–6139.
[22] D. Castillo-Castro, F. Correa, E. Aparicio, N. Amigo, A. Prada, J. Figueroa, R.I. González, E. Bringa, F.J. Valencia, Nanoporous amorphous carbon with exceptional ultra-high strength, Nanomaterials 13 (8) (2023) 1429.
[23] A. Dernov, M. Kowalik, A.C.T. van Duin, T. Dumitrică, Mapping the structural–mechanical landscape of amorphous carbon with ReaxFF molecular dynamics, J. Appl. Phys. 137 (6) (2025) 065107.
[24] J. Yu, X. Zhao, K. Xun, S. Zhang, L. Jiang, J. Ding, Machine learning-driven atomistic simulation of mechanical deformation in nanoporous amorphous carbon, Carbon 243 (2025) 120507.
[25] H. Patel, J. Kröner, M. Schwan, B. Milow, A. Rege, Molecular description of mechanical structure-property relationships of nanostructured porous carbon, J. Phys. Chem. C 128 (49) (2024) 21245–21252.
[26] A.P. Thompson, H.M. Aktulga, R. Berger, D.S. Bolintineanu, W.M. Brown, P.S. Crozier, P.J. in 't Veld, A. Kohlmeyer, S.G. Moore, T.D. Nguyen, R. Shan, M.J. Stevens, J. Tranchida, C. Trott, S.J. Plimpton, LAMMPS - a flexible simulation tool for particle-based materials modeling at the atomic, meso, and continuum scales, Comput. Phys. Comm. 271 (2022) 108171.
[27] S.J. Stuart, A.B. Tutein, J.A. Harrison, A reactive potential for hydrocarbons with intermolecular interactions, J. Chem. Phys. 112 (14) (2000) 6472–6486.
[28] D.W. Brenner, O.A. Shenderova, J.A. Harrison, S.J. Stuart, B. Ni, S.B. Sinnott, A second-generation reactive empirical bond order (REBO) potential energy expression for hydrocarbons, J. Phys.: Condens. Matter. 14 (4) (2002) 783–802.
[29] Z. Luo, S.A. Burrows, X. Fan, S.K. Smoukov, E.S. Boek, Virtual voids method to generate low-density microporous carbon structures using quenched molecular dynamics simulation, Carbon 183 (2021) 438–448.
[30] H. Wang, Q. Cao, Q. Peng, S. Liu, Atomistic study of mechanical behaviors of carbon honeycombs, Nanomaterials 9 (1) (2019) 109.
[31] A. Stukowski, Visualization and analysis of atomistic simulation data with OVITO–the Open Visualization Tool, Modelling Simul. Mater. Sci. Eng. 18 (1) (2010) 015012.
[32] A.A. Griffith, VI. The phenomena of rupture and flow in solids, Philos. Trans. R. Soc. Lond. Ser. A 221 (582–593) (1921) 163–198.
[33] N. Perez, Fracture mechanics, Kluwer Academic Publishers, Boston, Massachusetts, United States, 2004.
[34] G.R. Irwin, Analysis of stresses and strains near the end of a crack traversing a plate, J. Appl. Mech. 24 (3) (1957) 361–364.
[35] Y. Liu, W. Gong, X. Zhang, Numerical investigation of influences of porous density and strain-rate effect on dynamical responses of aluminum foam, Comput. Mater. Sci. 91 (2014) 223–230.
[36] G. Lu, G.Q. Lu, Z.M. Xiao, Mechanical properties of porous materials, J. Porous Mater. 6 (4) (1999) 359–368.
[37] T. Vo, B. He, M. Blum, A. Damone, P. Newell, Molecular scale insight of pore morphology relation with mechanical properties of amorphous silica using ReaxFF, Comput. Mater. Sci. 183 (2020) 109881.
[38] Y.O. Yildiz, A. Ahadi, M. Kirca, Strain rate effects on tensile and compression behavior of nano-crystalline nanoporous gold: A molecular dynamic study, Mech. Mater. 143 (2020) 103338.
[39] S. Liu, K. Duan, J. Feng, L. Li, X. Wang, Y. Hu, Z. Qin, The design of strongly bonded nanoarchitected carbon materials for high specific strength and modulus, Carbon 195 (2022) 387–394.
[40] Y. Wang, Z. Fan, P. Qian, T. Ala-Nissila, M.A. Caro, Structure and pore size distribution in nanoporous carbon, Chem. Mater. 34 (2) (2022) 617–628.
[41] J.C. Wong, H. Kaymak, S. Brunner, M.M. Koebel, Mechanical properties of monolithic silica aerogels made from polyethoxydisiloxanes, Microporous Mesoporous Mater. 183 (2014) 23–29.
[42] A. Rege, M. Itskov, A microcell-based constitutive modeling of cellulose aerogels under tension, Acta Mech. 229 (2) (2018) 585–593.
[43] J. Phalippou, T. Woignier, R. Rogier, Fracture toughness of silica aerogels, Le J. de Phys. Colloq. 50 (C4) (1989) C4–191–C4–196.
[44] A. Rege, Constitutive modeling of the densification behavior in open-porous cellular solids, Materials 14 (11) (2021) 2731.
[45] C. Ma, T. Ji, C.G. Robertson, R. Rajeshbabu, J. Zhu, Y. Dong, Molecular insight into the Mullins effect: irreversible disentanglement of polymer chains revealed by molecular dynamics simulations, Phys. Chem. Chem. Phys. 19 (29) (2017) 19468–19477.